
01 Jan 2023

Final-stage Densification Kinetics Of Direct Current–sintered ZrB₂

Austin D. Stanfield

Steven M. Smith

Suzana Filipović

Nina Obradović

et. al. For a complete list of authors, see https://scholarsmine.mst.edu/matsci_eng_facwork/3203

Follow this and additional works at: https://scholarsmine.mst.edu/matsci_eng_facwork

 Part of the [Ceramic Materials Commons](#)

Recommended Citation




A. D. Stanfield et al., "Final-stage Densification Kinetics Of Direct Current–sintered ZrB₂," *Journal of the American Ceramic Society*, Wiley, Jan 2023.

The definitive version is available at <https://doi.org/10.1111/jace.19212>

This Article - Journal is brought to you for free and open access by Scholars' Mine. It has been accepted for inclusion in Materials Science and Engineering Faculty Research & Creative Works by an authorized administrator of Scholars' Mine. This work is protected by U. S. Copyright Law. Unauthorized use including reproduction for redistribution requires the permission of the copyright holder. For more information, please contact scholarsmine@mst.edu.

RESEARCH ARTICLE

Final-stage densification kinetics of direct current–sintered ZrB₂

Austin D. Stanfield^{1,4}  | Steven M. Smith¹ | Suzana Filipović²  |
 Nina Obradović²  | Vladimir Buljak³ | Gregory E. Hilmas¹ |
 William G. Fahrenholtz¹ 

¹Materials Science and Engineering,
 Missouri University of Science and
 Technology, Rolla, Missouri, USA

²Institute of Technical Sciences, Serbian
 Academy of Sciences and Arts, Belgrade,
 Serbia

³Strength of Materials Department,
 Mechanical Engineering Faculty,
 University of Belgrade, Belgrade, Serbia

⁴Savannah River National Laboratory,
 Aiken, SC, USA

Correspondence

William G. Fahrenholtz, Missouri
 University of Science and Technology,
 Materials Science and Engineering, Rolla,
 MO 65409, USA.
 Email: billf@mst.edu

Editor's Choice

The Editor-in-Chief recommends this
 outstanding article.

Funding information

U.S. National Science Foundation,
 Grant/Award Number: CMMI 1902069

Abstract

Final-stage sintering was analyzed for nominally phase pure zirconium diboride synthesized by borothermal reduction of high-purity ZrO₂. Analysis was conducted on ZrB₂ ceramics with relative densities greater than 90% using the Nabarro–Herring stress–directed vacancy diffusion model. Temperatures of 1900°C or above and an applied uniaxial pressure of 50 MPa were required to fully densify ZrB₂ ceramics by direct current sintering. Ram travel data were collected and used to determine the relative density of the specimens during sintering. Specimens sintered between 1900 and 2100°C achieved relative densities greater than 97%, whereas specimens sintered below 1900°C failed to reach the final stage of sintering. The average grain size ranged from 1.0 to 14.7 μm. The activation energy was calculated from the slope of an Arrhenius plot that used the Kalish equation. The activation energy was 162 ± 34 kJ/mol, which is consistent with the activation energy for dislocation movement in ZrB₂. The diffusion coefficients for dislocation motion that controls densification were 5.1 × 10⁻⁶ cm²/s at 1900°C and 5.1 × 10⁻⁵ cm²/s at 2100°C, as calculated from activation energy and average grain sizes. This study provides evidence that the dominant mechanism for final-stage sintering of ZrB₂ ceramics is dislocation motion.

KEYWORDS

activation energy, densification, modeling, sintering, ZrB₂

1 | INTRODUCTION

Zirconium diboride (ZrB₂) is classified as an ultrahigh temperature ceramic (UHTC) due to its melting temperature of 3250°C. In addition to its high melting temperature, interest in ZrB₂ is driven by properties such as strength (>500 MPa),¹ hardness (>20 GPa),^{2,3} thermal conductivity (as high as 140 W/m K),^{4,5} and chemical inertness,^{6,7} making ZrB₂ a candidate material for applications such as leading edges for hypersonic aerospace vehicles,^{8,9} refractory linings,¹⁰ high-temperature electrodes,¹¹ and high-speed

cutting tools.¹² These properties are due, in part, to the complex combination of different types of bonding. ZrB₂ has a hexagonal crystal structure (space group 191) with alternating layers of metallicly bonded, close-packed zirconium atoms, and covalently bonded boron rings. The bonding between the two types of layers is ionocovalent.¹³

Densifying phase pure ZrB₂ is difficult due to strong covalent bonding and low self-diffusion coefficients. Sintering to full density generally requires temperatures above 1900°C and applied pressures greater than 32 MPa.¹⁴ For these reasons, hot pressing (HP), direct current

sintering (DCS), and variants of both employing in situ reactions have become the favored sintering method for producing phase pure UHTCs with relative density above 90%.^{15–19} For the intermediate stage of sintering ($0.65 < \rho_{\text{relative}} < 0.90$) of the Group IV diborides, activation energies that have been reported range from 140 to 695 kJ/mol for ZrB₂, 56 to 774 kJ/mol of TiB₂, and 96 kJ/mol for HfB₂.^{5,20–23} In general, studies have concluded that finer initial particle size and increased pressures reduced activation energies, even though the value of activation energy should only depend on the densification mechanism. For the intermediate stage of sintering, Lonergan reported that grain boundary diffusion was the dominant mechanism in reactively hot pressed ZrB₂ below 2000°C with an activation energy of 241 kJ/mol, but lattice diffusion became the dominant mechanism above 2000°C with an activation energy of 695 kJ/mol.²¹ Kalish studied the kinetics of the final stage of densification under extreme pressures (800 MPa) for HfB₂ and reported an activation energy of 96 kJ/mol. Kalish suggested that the mechanism could be dislocation flow because the activation energy was sufficiently low, but no other evidence of the mechanism was provided. Kalish ultimately concluded that interstitial diffusion of B or grain boundary diffusion of Hf was the predominant mechanism in the final stage of densification of HfB₂.⁵ Since then, several studies have reported dislocation motion in the borides.^{24–29} Koval'chenko studied densification kinetics of molybdenum and tungsten borides and reported that activation energies were independent of pressure, which is indicative of the dislocation glide process. Koval'chenko concluded that dislocation movement was limited by the self-diffusion of the metallic species in the metallic sublattice.²⁸ Bhakhri estimated an activation energy for dislocation movement in ZrB₂ of 154 ± 96 kJ/mol using indentation experiments and assuming the Burger vector to be along the $\langle 1000 \rangle$ direction.²⁴

This study investigates the mechanism of the final stage of sintering for nominally phase pure ZrB₂ by applying the Nabarro–Herring stress-directed vacancy diffusion model to ram travel data collected during DCS.

1.1 | Densification model

The final stage of densification was analyzed by the Nabarro–Herring stress-directed vacancy diffusion model.^{30,31} This model evaluates the movement of vacancies from crystal faces under tension to crystal faces under compression and the subsequent transfer of atoms from a crystal face under compression to a crystal face under tension. This model is also known as vacancy creep and was used by Kalish to describe the final-stage

densification of HfB₂ during HP.³² Both HP and DCS rely on pressure-assisted densification, which is captured by

$$\ln \left[\ln \left(\frac{1-f_p}{1-f_{p0}} \right) \right] - \ln \left[\exp \left(\frac{\sigma \Omega_n}{kT} \right) - \exp \left(-\frac{\sigma \Omega_n}{kT} \right) \right] = \ln \frac{Dt}{d^2} - \frac{Q}{RT} \quad (1)$$

$$\sigma = \frac{\sigma_a}{1-f_p^{2/3}} \quad (2)$$

where f_p is pore fraction, f_{p0} is initial pore fraction, σ is stress corrected for the effect of porosity by the Spriggs correction factor (Equation 2), σ_a is the uniaxially applied stress during DCS,³³ Ω_n is atomic volume of species n , k is the Boltzmann constant, T is absolute temperature, D is the diffusion coefficient, t is time, d is grain size, Q is activation energy for diffusion, and R is the universal gas constant. A value of 15.4 \AA^3 was used for the atomic volume (Ω_n).³⁴ Although this equation does not account for current effects, those are believed to be negligible in the present study and left for future investigation.

To determine the activation energy, the left-hand side of Equation (1) can be rewritten as Equation (3) and plotted as a function of inverse temperature with the resulting linear trend having a slope of Q/R . The right hand side of Equation (1) can also be rewritten as Equation (4) and used to calculate the diffusion coefficient:

$$G = \ln \left(\frac{\ln \frac{1-f_{p0}}{1-f_p}}{e^{\frac{\sigma \Omega_n}{kT}} - e^{-\frac{\sigma \Omega_n}{kT}}} \right) \quad (3)$$

$$G = \ln \frac{Dt}{d^2} - \frac{Q}{RT} \quad (4)$$

1.2 | Finite-element model

A numerical model was used to analyze the sintering as a transient process using the finite element method with a combination of applied pressure and temperature within an uncoupled thermomechanical simulation. The inputs to the numerical model were the temperature and the applied pressure profiles. The phenomenological approach of Olevsky³⁵ was adopted whereby the material was treated as a continuum, that is, porosity was not modeled directly but averaged in the sense that it was included into the analysis through relative density. The relative density was related to the volumetric strain by the following equation:

$$\rho = \rho_0 e^{-(\epsilon_{xx} + \epsilon_{yy} + \epsilon_{zz})} \quad (5)$$

with ρ_0 being the initial relative density.

The constitutive equation was a nonlinear viscous incompressible model in which the total strain rate was decomposed into three parts: thermal, elastic, and viscous strain:

$$\dot{\epsilon} = \dot{\epsilon}^{\text{th}} + \dot{\epsilon}^{\text{el}} + \dot{\epsilon}^{\text{vs}} \quad (6)$$

The constitutive equation was thus of the following form:

$$\dot{\sigma} = C (\dot{\epsilon} - \dot{\epsilon}^{\text{th}} - \dot{\epsilon}^{\text{vs}}) \quad (7)$$

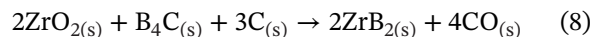
where $\dot{\sigma}$ is the applied stress, and C is the elasticity tensor. For this study, isotropic elastic behavior was assumed. This assumption allowed C to be defined using two independent constants, here specifically selected as the Young modulus being equal to 440 GPa, and Poisson's ratio equal to 0.2.³⁶ Isotropic behavior was also assumed for thermal expansion. Hence, only one thermal expansion coefficient was needed and the value was assumed to be $8 \times 10^{-6}/\text{K}$. For the calculation of the viscous part of the strain rate, four additional constants were determined by fitting of the data.³⁵

The constitutive model was implemented through a user subroutine within commercial finite element software (Abaqus). Parameters entered into the governing equations of the model were quantified to match the curves of averaged relative density as a function of time collected during densification. For assessment of the parameters, an inverse analysis was used.^{37,38} The procedure is not detailed here for brevity but was based on minimization of the discrepancy function between measured and computed curves. An uncoupled heat-transfer simulation was first performed to obtain temperature fields as a function of time, which were then used as the thermal conditions in the sintering simulations.

2 | EXPERIMENTAL PROCEDURES

Nominally phase pure ZrB_2 was synthesized by boro/carbothermal reduction of ZrO_2 (Reactor Grade, 99.7%, Hf < 75 ppm, Materion, Mayfield Heights, OH, USA) according to Equation (8). ZrO_2 and carbon black (BP1100, Cabot, Alpharetta, GA, USA) were combined by high-energy ball milling for 2 h in a WC jar with WC media as described in our previous studies.^{39–41} The level of WC contamination was determined to be 0.02 wt.% based on mass measurements of the jar and media before and after milling. The milled powder was then mixed with B_4C (H.S. Grade, H.C. Starck, Newton, MA, USA) by ball milling in acetone for 4 h with zirconia media in a high-density polyethylene bottle. To account for

B loss due to the volatilization of various boron oxides during reaction, 13 wt.% excess B_4C was added during milling:



The mixture was dried by rotary evaporation, lightly ground with an alumina mortar and pestle to break agglomerates and pressed into cylindrical 50 g pellets 4 cm in diameter and approximately 1 cm thick. Pellets were reacted in a resistively heated graphite element furnace (HP50-7010G, Thermal Technology, Santa Rosa, CA, USA) under mild vacuum (~ 3 Pa) with a $10^\circ\text{C}/\text{min}$ heating rate with a 4 h hold at 1650°C . The oxygen content of the resulting powder was measured by the inert gas fusion method (TS500, LECO, St. Joseph, MI, USA). Before densification, a 3 wt.% super addition of phenolic resin (GP 2074, Georgia-Pacific, Atlanta, GA, USA) was added as a carbon source by ball milling in acetone for 4 h with ZrB_2 media. Powder was dried by rotary evaporation and then densified by DCS (DSC10 Thermal Technology, Santa Rosa, CA, USA) under mild vacuum (~ 2 Pa) in a 20 mm diameter graphite die. Specimens were heated at $100^\circ\text{C}/\text{min}$ under 15 MPa applied pressure from room temperature to 1650°C . Specimens were held at that temperature for 5 min to promote removal of oxygen impurities from particle surfaces.^{42,43} After the hold, pressure was increased to 50 MPa, and specimens were heated at $100^\circ\text{C}/\text{min}$ to the final densification temperature where temperature was held for 15 min. The furnace was then cooled at a rate of $100^\circ\text{C}/\text{min}$, and the pressure was released at 1500°C . X-ray diffraction (XRD; PANalytical X'Pert Pro, Malvern Panalytical Ltd., Royston, UK) analysis was used to identify phases present in the as-reacted powders and after final densification. Lattice parameters were determined using the Rietveld refinement (RIQAS4, Materials Data Incorporated, Livermore, CA, USA) of XRD data, which were then used to calculate crystallographic density. Bulk density of the final specimens was determined by Archimedes' principle. Time-dependent relative density (ρ_t) was calculated from the final bulk densities of the specimens and ram travel data collected during DCS according to the following equation:

$$\rho_t = \frac{\rho}{\left(1 + \frac{L_t}{L_f}\right)} \quad (9)$$

where L_t is specimen thickness at time t , and L_f is final thickness. The effects of thermal expansion of the ram were subtracted from the measured travel by recording ram travel for a run with an identical ramp, but without a specimen in the die.

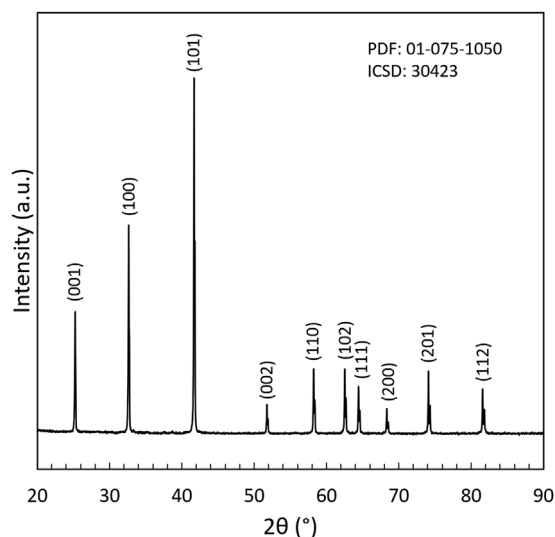


FIGURE 1 X-ray diffraction (XRD) pattern of ZrB_2 densified at 2100°C.

Scanning electron microscopy (SEM; eLine Plus, Raith GmbH, Dortmund, Germany) was performed using a 15 kV accelerating voltage in backscattered electron mode on cross-sectioned specimen. Grain size was determined by measuring the Feret diameter from SEM micrographs in digital image-processing software (ImageJ, National Institutes of Health, Bethesda, MD, USA). A minimum of 400 grains were measured for each reported value. Micro-Raman spectroscopy (LabRAM ARAMIS, HORIBA Jobin Yvon, Edison, NJ, USA) was used to identify secondary phases.

3 | RESULTS AND DISCUSSION

ZrB_2 was the only phase detected by XRD in all specimens after synthesis and densification. A representative XRD pattern of a densified ceramic is shown in Figure 1, but nominally phase pure ZrB_2 was the only phase detected in all synthesized powders and densified ceramics.

The lattice parameters of the densified ceramics, as calculated by Rietveld refinement, were $a = 3.1685 \pm 0.0004 \text{ \AA}$ and $c = 3.5309 \pm 0.0002 \text{ \AA}$, with the variabilities being error from the Rietveld fit. Using the lattice parameters, crystallographic density was $6.103 \pm 0.001 \text{ g/cm}^3$ calculated for ZrB_2 . Due to the low Hf content ($<75 \text{ ppm}$) of the starting ZrO_2 precursor, the Hf content was assumed to be negligible in the calculation of theoretical density of the final ZrB_2 .

Microstructure analysis revealed that the ceramics contained a small volume fractions of porosity and a secondary phase (Figure 2). The predominant phase was ZrB_2 , which appears as the gray phase in the micrographs. A small vol-

ume fraction of two types of inclusions was noted. First, the black circular inclusions with charging around the perimeter are porosity. Note that some additional angular voids were also present. The angular voids are consistent with grain pullout that occurred during polishing and were not considered further. The circular black inclusions that do not have charging around the perimeter were residual B_4C that was not consumed in the reaction process. The composition of the B_4C inclusions was verified by micro-Raman spectroscopy (not shown) similar to observations in our previous studies.^{44,45}

A summary of the grain sizes and densities for all of the sintered specimens is provided in Table 1 along with specimen identification and densification temperatures. Among the ceramics produced, DCS_2100 had the largest average grain size at $14.7 \pm 6.6 \text{ }\mu\text{m}$. The increased average grain size and higher standard deviation may be due to rapid grain growth caused by the higher densification temperature, which resulted in a lower relative density of 97.4% compared to 98.0% for DCS_2000 and 99.2% for DCS_2050.

Figure 3 shows the relative density as a function of time for different sintering temperatures. Densification data were collected from 1800 to 2100°C, but a distinct difference was noted in the densification rate and final density between specimens sintered above 1900°C compared to those sintered below that temperature. Results from DCS_1800 and DCS_1850 were not included in the final analysis of the mechanism(s) because the relative densities were too low and the specimens did not exhibit sufficient final-stage sintering behavior for analysis. Specimens sintered at 1900°C and above achieved relative densities of 97% or higher and had a significant portion of their densification curves above 90%, which indicated that they had reached the final stage of densification. Figure 4 shows the value of G calculated using Equation (3) as a function of time for specimens sintered at and above 1900°C. The activation energy was calculated from the slope of the plot of G as a function of inverse temperature (Figure 5). Using four different densities, ranging from 95.0% to 97.3%, the average activation energy was determined to be $168 \pm 24 \text{ kJ/mol}$. This value is in good agreement with the activation energy estimated for dislocation movement reported by Bhakhri.²⁴ The activation energy measured for final-stage densification in the present study is significantly lower than activation energies for grain boundary diffusion ($\sim 250 \text{ kJ/mol}$) and lattice diffusion ($\sim 700 \text{ kJ/mol}$) identified by Lonergan for intermediate stage densification of ZrB_2 ,²¹ providing confidence that final-stage sintering is controlled by a different process.

The dislocation diffusion coefficient was calculated from the activation energy and grain size for 1900 and 2100°C according to Equation (3). Final grain sizes were used as it was assumed that no significant grain growth

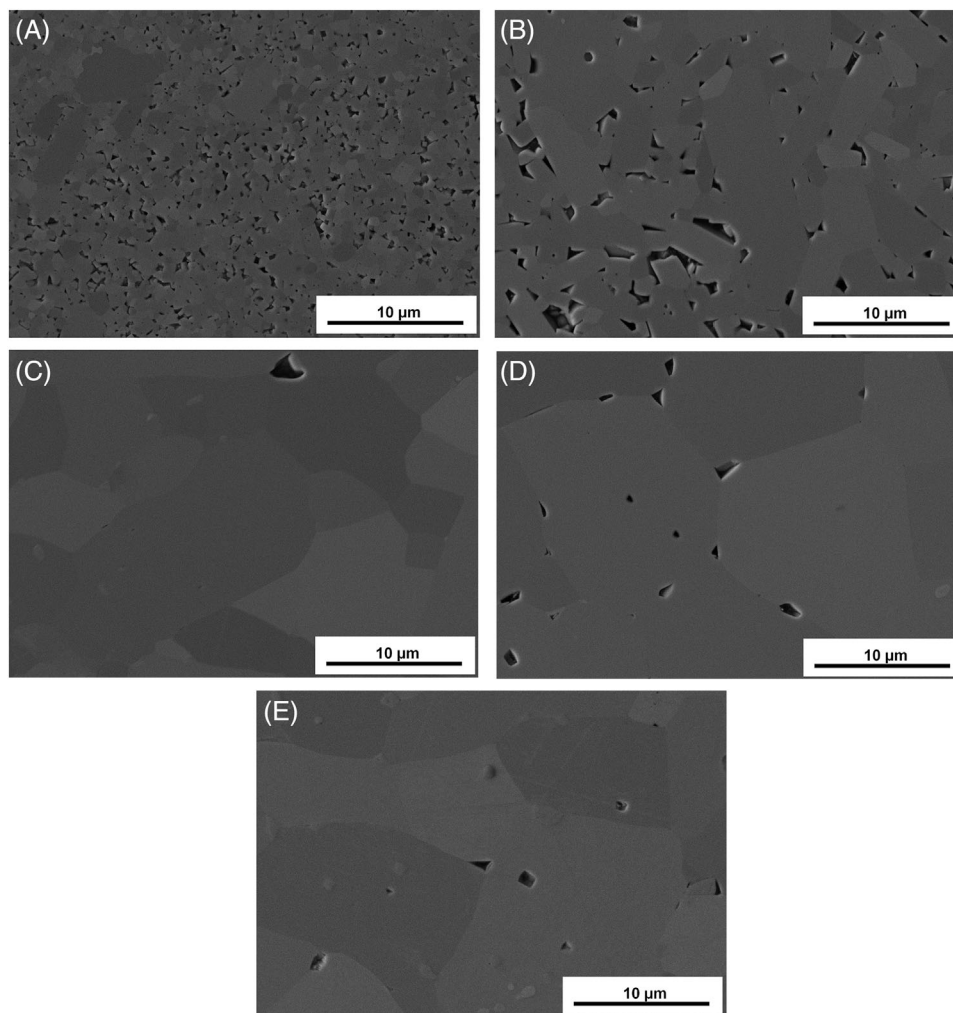


FIGURE 2 Scanning electron microscopy (SEM) micrographs of specimens sintered at (A) 1900°C, (B) 1950°C, (C) 2000°C, (D) 2050°C, and (E) 2100°C. Note that all images are at the same magnification for consistency. Additional magnifications are shown in Figures S1 and S2.

TABLE 1 Summary of densification temperature, density, and average grain size for sintered specimens.

Specimen ID	Temperature (°C)	ρ_{bulk} (g/cm ³)	ρ_{relative} (%)	Average grain size (μm)
DCS_1800	1800	5.47	89.6	1.0 ± 0.5
DCS_1850	1850	5.54	90.8	1.2 ± 0.6
DCS_1900	1900	5.94	97.3	1.4 ± 0.9
DCS_1950	1950	6.02	98.7	2.7 ± 1.6
DCS_2000	2000	5.98	98.0	8.2 ± 4.3
DCS_2050	2050	6.06	99.2	11.7 ± 5.6
DCS_2100	2100	5.94	97.4	14.7 ± 6.6

occurred upon cooling from the sintering temperature. The diffusion coefficient was 5.1×10^{-6} cm²/s at 1900°C and 5.1×10^{-5} cm²/s at 2100°C. The 1900°C diffusion coefficient is similar to the value of 2.4×10^{-6} cm²/s calculated by Kalish for final-stage sintering of HfB₂.³² The dislo-

cation diffusion coefficients are also consistent with self-diffusion in Zr, which validates Koval'chenko's conclusion that dislocation movement is limited by the self-diffusion of the metallic species in the metallic sublattice.^{28,46} Taken together, the values of the diffusion coefficients and activation energies are consistent with the final stage of densification of ZrB₂ being controlled by stress-assisted dislocation motion. Future studies utilizing analysis transmission electron microscopy could confirm this mechanism.

Figure 6 compares the computed and experimental, averaged relative densities as a function of sintering time for densification at 1900°C. The two curves matched reasonably well. Aside from the overall global response of the material in terms of the change in averaged relative density with sintering time, the numerical model also provides insight into local distribution of relative density as well as the local stresses and strains during the sintering process. The model indicates thermal strain starts to rise

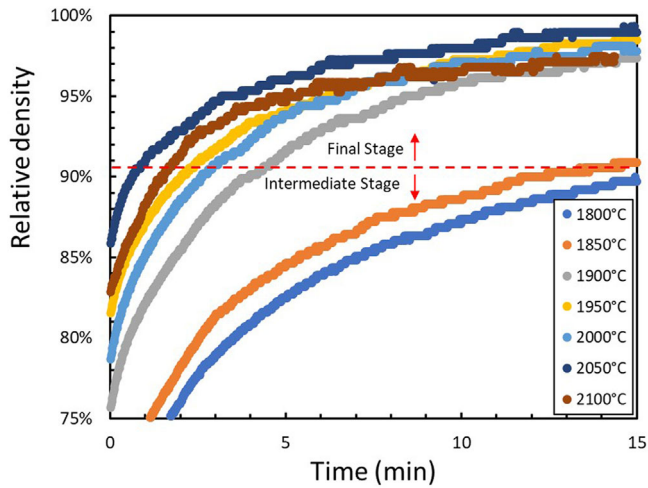


FIGURE 3 Relative densities as a function of sintering time at indicated isothermal holds.

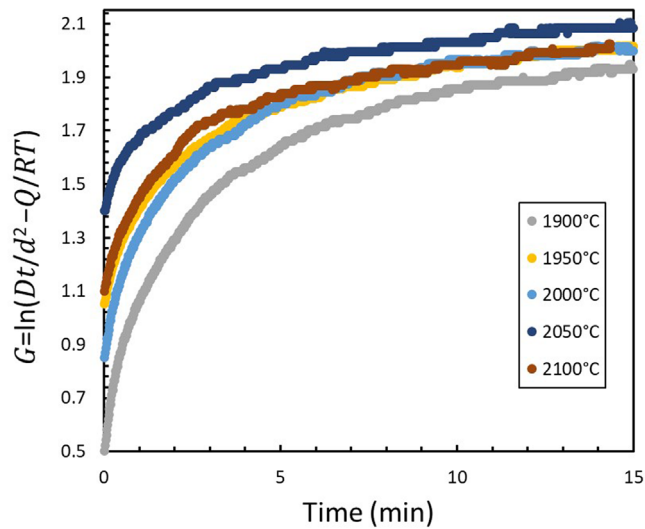


FIGURE 4 Time-dependent densification data plotted as G calculated using Equation (3).

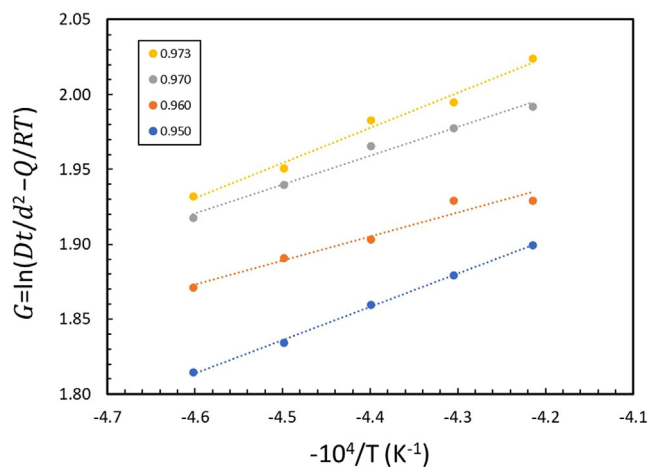


FIGURE 5 Temperature dependence of the G function calculated using Equation (3) for relative densities in the range of 0.950–0.973.

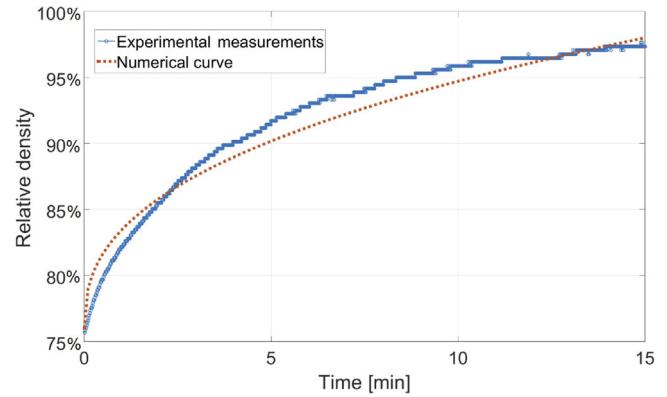


FIGURE 6 Relative density as a function of time curves for sintering at 1900°C comparing results from experiments and the numerical simulation.

during initial densification, which, in turn, triggers the elastic strain to generate stresses to satisfy the equilibrium. As deformation continues, the viscous component of the strain starts to grow and becomes dominant in the later stages of the sintering process, which is consistent with the dislocation creep mechanism determined from the analysis of experimental results. In addition, the transition from one mechanism to another one is described by the model parameters and can be quantified from the distribution of internal stresses and/or relative densities throughout the specimen by examining microstructures at intermediate times during sintering.


4 | CONCLUSIONS

Final-stage densification kinetics was studied in nominally phase pure ZrB_2 . Temperatures above 1850°C were needed to reach the final stage of densification. Relative densities of >97% were achieved for sintering temperatures of 1900°C and above with an applied stress of 50 MPa. The activation energy was determined to be 168 ± 24 kJ/mol, which was consistent with the activation energy of dislocation movement as calculated from indentation experiments. The diffusion coefficient ranged from 5.1×10^{-6} cm²/s at 1900°C to 5.1×10^{-5} cm²/s at 2100°C. A numerical model used experimental data to show that the mechanism active during the final stage of sintering was consistent with the dislocation motion mechanism proposed herein. Although grain boundary and lattice diffusion have previously been identified as controlling mechanisms for the intermediate stage of densification in ZrB_2 , this study provides evidence that dislocation motion is critical for ZrB_2 ceramics to reach full density during final stage sintering.

ACKNOWLEDGMENTS

This research was funded by the National Science Foundation (CMMI-1902069). The authors would like to thank the Advanced Materials Characterization Laboratory at Missouri S&T.

ORCID

Austin D. Stanfield  <https://orcid.org/0000-0001-7325-2100>

Suzana Filipović  <https://orcid.org/0000-0001-6383-8327>

Nina Obradović  <https://orcid.org/0000-0002-7993-293X>

William G. Fahrenholtz  <https://orcid.org/0000-0002-8497-0092>

REFERENCES

- Zapata-Solvas E, Jayaseelan DD, Lin H-T, Brown P, Lee WE. Mechanical properties of ZrB₂- and HfB₂-based ultra-high temperature ceramics fabricated by spark plasma sintering. *J Eur Ceram Soc.* 2013;33(7):1373–86.
- Guo S, Nishimura T, Kagawa Y. Preparation of zirconium diboride ceramics by reactive spark plasma sintering of zirconium hydride–boron powders. *Scr Mater.* 2011;65(11):1018–21.
- Csanádi T, Grasso S, Kovalčíková A, Dusza J, Reece M. Nanohardness and elastic anisotropy of ZrB₂ crystals. *J Eur Ceram Soc.* 2016;36(1):239–42.
- Fridlender BA, Neshpor VS, Ordan'yan SS, Unrod VI. Thermal conductivity and thermal diffusivity of binary alloys of the ZrC–ZrB₂ system at high temperatures. *Teplofiz Vysok Temp.* 1979;17(6):1210–5.
- Stanfield AD, Hilmas GE, Fahrenholtz WG. Effects of Ti, Y, and Hf additions on the thermal properties of ZrB₂. *J Eur Ceram Soc.* 2020;40(12):3824–8.
- Binner J, Porter M, Baker B, Zou J, Venkatachalam V, Diaz VR, et al. Selection, processing, properties, and applications of ultra-high temperature ceramic matrix composites, UHTCMCs—a review. *Int Mater Rev.* 2020;65:389–444
- Ni D, Cheng Y, Zhang J, Liu J-X, Zou J, Chen B, et al. Advances in ultra-high temperature ceramics, composites, and coatings. *J Adv Ceram.* 2022;11:1–56.
- Clougherty EV, Kalish D, Peters ET. Research and development of refractory oxidation-resistant diboride. Technical Report AFML-TR-68-190, Air Force Materials Laboratory, Wright Patterson Air Force Base; 1968.
- Opeka MM, Talmy IG, Zaykoski JA. Oxidation-based materials selection for 2000°C + hypersonic aerosurfaces: theoretical considerations and historical experience. *J Mater Sci.* 2004;39(19):5887–904.
- Kaji N, Shikano H, Tanaka I. Development of ZrB₂-graphite protective sleeve for submerged nozzle. *Taikabutsu Overseas.* 1994;14(2):39–43.
- Stucker BE. Rapid prototyping of zirconium diboride/copper electrical discharge machining electrodes (PhD dissertation). College Station: Texas A&M University; 1997.
- Murata Y. Cutting tool tips and ceramics containing hafnium nitride and zirconium diboride. U.S. Patent Number 3,487,594; January 6, 1970.
- Spear KE. Chemical bonding in AlB₂-type borides. *J Less-Common Met.* 1976;47:195–201
- Sonber JK, Suri AK. Synthesis and consolidation of zirconium diboride. *Adv Appl Ceram.* 2011;110(6):321–34.
- Zou J, Zhang GJ, Vleugels J, Van der Biest O. High temperature strength of hot pressed ZrB₂-20 vol% SiC ceramics based on ZrB₂ starting powders prepared by different carbo/borothermal reduction routes. *J Eur Ceram Soc.* 2013;33(10):1609–14.
- Guo W-M, Zhang G-J. Reaction processes and characterization of ZrB₂ powder prepared by boro/carbothermal reduction of ZrO₂ in vacuum. *J Am Ceram Soc.* 2009;92:264–7.
- Chamberlain AL, Fahrenholtz WG, Hilmas GE. Reactive hot pressing of zirconium diboride. *J Eur Ceram Soc.* 2009;29(16):3401–8.
- Venugopal S, Paul A, Vaidhyanathan B, Binner JGP, Heaton A, Brown PM. Synthesis and spark plasma sintering of sub-micron HfB₂: effect of various carbon sources. *J Eur Ceram Soc.* 2014;34(6):1471–9.
- Fahrenholtz WG, Hilmas GE, Li R. Densification of ultra-refractory transition metal diboride ceramics. *Sci Sinter.* 2020;52(1):1–14.
- Karthiselva NS, Kashyap S, Yadav D, Murty BS, Bakshi SR. Densification mechanisms during reactive spark plasma sintering of titanium diboride and zirconium diboride. *Philos Mag.* 2017;97(19):1588–609.
- Lonergan JM, Fahrenholtz WG, Hilmas GE. Sintering Mechanisms and kinetics for reaction hot-pressed ZrB₂. *J Am Ceram Soc.* 2015;98(8):2344–51.
- Khanra AK, Godkhindi MM, Pathak LC. Sintering behaviour of ultra-fine titanium diboride powder prepared by self-propagating high-temperature synthesis (SHS) technique. *Mater Sci Eng A.* 2007;454:281–7.
- Ouabdesselam M, Munir ZA. The sintering of combustion-synthesized titanium diboride. *J Mater Sci.* 1987;22(5):1799–807.
- Bhakhri V, Wang J, Ur-Rehman N, Ciurea C, Giuliani F, Vandeperre LJ. Instrumented nanoindentation investigation into the mechanical behavior of ceramics at moderately elevated temperatures. *J Mater Res.* 2012;27(1):65–75.
- Haggerty JS, Lee DW. Plastic deformation of ZrB₂ single crystals. *J Am Ceram Soc.* 1971;54(11):572–6.
- Ghosh D, Subhash G, Bourne GR. Room-temperature dislocation activity during mechanical deformation of polycrystalline ultra-high-temperature ceramics. *Scr Mater.* 2009;61(11):1075–8.
- Sekido N, Ohmura T, Perepezko JH. Mechanical properties and dislocation character of YB₄ and YB₆. *Intermetallics.* 2017;89:86–91.
- Koval'chenko MS, Bodrova LG. Densification kinetics of higher molybdenum and tungsten borides in hot pressing. *Sov Powder Metall Met Ceram.* 1975;14(6):469–73.
- Patel M, Singh V, Reddy JJ, Prasad VVB, Jayaram V. Densification mechanisms during hot pressing of ZrB₂-20 vol.% SiC composite. *Scr Mater.* 2013;69(5):370–3.
- Mott NF, Nabarro FRN. Conference on strength of solids. London: Physical Society; 1948. p. 1.
- Herring C. Diffusional viscosity of a polycrystalline solid. *J Appl Phys.* 1950;21(5):437–45.

32. Kalish D, Clougherty EV. Densification mechanisms in high-pressure hot-pressing of HfB_2 . *J Am Ceram Soc.* 1969;52(1):26–30.
33. Spriggs RM, Vasilos T. Functional relation between creep rate and porosity for polycrystalline ceramics. *J Am Ceram Soc.* 1964;47(1):47–8.
34. Wang J. Processing and deformation of ZrB_2 (PhD dissertation). London: Imperial College London; 2013.
35. Olevsky EA. Theory of sintering: from discrete to continuum. *Mater Sci Eng R Rep.* 1998;23(2):41–100.
36. Levine SR, Opila EJ, Halbig MC, Kiser JD, Singh M, Salem JA. Evaluation of ultra-high temperature ceramics for aer propulsion use. *J Eur Ceram Soc.* 2002;22:2757–67.
37. Buljak V, Maier G. Proper orthogonal decomposition and radial basis functions in material characterization based on instrumented indentation. *Eng Struct.* 2011;33(2):492–501.
38. Buljak V. Inverse analyses with model reduction: proper orthogonal decomposition in structural mechanics. Berlin: Springer Science & Business Media; 2011.
39. Feng L, Fahrenholtz WG, Hilmas GE. Two-step synthesis process for high-entropy diboride powders. *J Am Ceram Soc.* 2020;103(2):724–30.
40. Feng L, Monteverde F, Fahrenholtz WG, Hilmas GE. Superhard high entropy AlB_2 -type diboride ceramics. *Scr Mater.* 2021;199:113855.
41. Feng L, Fahrenholtz WG, Brenner DW. High entropy ultra-high temperature borides and carbides: a new class of materials for extreme environments. *Annu Rev Mater Res.* 2021;51:165–85.
42. Fahrenholtz WG, Hilmas GE, Zhang SC, Zhu S. Pressureless sintering of zirconium diboride: particle size and additive effects. *J Am Ceram Soc.* 2008;91(5):1398–404.
43. Neuman EW, Hilmas GE, Fahrenholtz WG. Strength of zirconium diboride to 2300°C. *J Am Ceram Soc.* 2013;96(1):47–50.
44. Harrington G, Hilmas GE, Fahrenholtz WG. Effect of carbon and oxygen on the densification and microstructure of hot pressed zirconium diboride. *J Am Ceram Soc.* 2013;96:3622–3630.
45. Brown-Shaklee HJ, Fahrenholtz WG, Hilmas GE. Densification behavior and thermal properties of hafnium diboride with additions of boron carbide. *J Am Ceram Soc.* 2012;95:2035–43.
46. Naik MC, Agarwala RP. Self and impurity diffusion in alpha-zirconium. *Acta Metall.* 1967;15(9):1521–5.

SUPPORTING INFORMATION

Additional supporting information can be found online in the Supporting Information section at the end of this article.

How to cite this article: Stanfield AD, Smith SM, Filipović S, Obradović N, Buljak V, Hilmas GE, et al. Final-stage densification kinetics of direct current-sintered ZrB_2 . 2023;106:5654–5661.
<https://doi.org/10.1111/jace.19212>